Delft University of Technology

Reliable Work Function Determination of Multicomponent Surfaces and Interfaces
The Role of Electrostatic Potentials in Ultraviolet Photoelectron Spectroscopy

Schultz, Thorsten; Lenz, Thomas; Kotadiya, Naresh; Heimel, Georg; Glasser, Gunnar; Berger, Rüdiger; Blom, Paul W.M.; Amsalem, Patrick; de Leeuw, Dago M.; Koch, Norbert

Important note
To cite this publication, please use the final published version (if applicable).
Please check the document version above.

Reliable Work Function Determination of Multicomponent Surfaces and Interfaces: The Role of Electrostatic Potentials in Ultraviolet Photoelectron Spectroscopy

Thorsten Schultz, Thomas Lenz, Naresh Kotadiya, Georg Heimel, Gunnar Glasser, Rüdiger Berger, Paul W. M. Blom, Patrick Amsalem, Dago M. de Leeuw, and Norbert Koch*

Ultraviolet photoelectron spectroscopy (UPS) is a key technique to determine the work function (Φ) of surfaces by measuring the secondary-electron cut-off (SECO). However, the interpretation of SECO spectra as obtained by UPS is not straightforward for multicomponent surfaces, and it is not comprehensively understood to what extent the length scale of inhomogeneity impacts the SECO. Here, this study unravels the physics governing the energy distribution of the SECO by experimentally and theoretically determining the electrostatic landscape above surfaces with defined patterns of Φ. For such samples, the measured SECO spectra exhibit actually two cut-offs, one representing the high Φ surface component and the other one corresponding to an area-averaged Φ value. By combining Kelvin probe force microscopy and electrostatic modeling, it is quantitatively demonstrated that the electrostatic potential of the high Φ areas leads to an additional energy barrier for the electrons emitted from the low Φ areas. Theoretical predictions of the induced energy barrier dependence on the Φ-pattern length scale and sample bias are further experimentally verified. These findings establish a solid base for reliable SECO interpretation of heterogeneous surfaces and improved reliability of interfacial energy-level diagrams from UPS experiments.

1. Introduction

The electronic structure of functional materials and their interfaces as used in electronic and optoelectronic devices is decisive for their fundamental function and efficiency. For instance, the level offset between valence and conduction band edges at a semiconductor heterojunction determines whether it facilitates energy transfer or charge separation, and the energy difference between an electrode's Fermi level and the frontier levels of a semiconductor determines the efficiency of charge injection. To select materials to achieve a targeted device functionality and to optimize efficiency, researchers and engineers often refer to published material parameters, such as ionization energy, electron affinity, and work function. These are then connected assuming a constant electrostatic potential across the interface (vacuum-level alignment), resulting in a hypothetical energy-level diagram of the device. While it is known that numerous interfacial phenomena, such as charge transfer,[1,2] bond formation,[3] and electron tail push-back[4,5] give rise to electrostatic potential changes at an actual interface of materials, the level estimation assuming vacuum-level alignment is a useful first-order approximation. This requires that above-mentioned material parameters are reliable. Nowadays, ultraviolet photoelectron spectroscopy (UPS) is the most frequently employed technique to determine the work function (Φ) of electronic and functional materials, and with it as input also the ionization energy and electron affinity (with an additional inverse photoemission experiment). There are, however, unresolved issues regarding the reliability and fundamental understanding of Φ determination with UPS, particularly with regard to samples with inhomogeneous surfaces and nanostructured materials. For example, a shift of Φ upon variation of surface composition could be interpreted as due to band bending,[6–8] and there are instances when more than one Φ value could be derived from UPS spectra.[9–11] In this contribution, we attend to these issues and provide experimental and theoretical insight that will allow an improved use of Φ as important material and sample parameter.

T. Schultz, Dr. G. Heimel, Dr. P. Amsalem, Prof. N. Koch
Humboldt Universität zu Berlin
Institut für Physik and IRIS Adlershof
Brook-Taylor-Straße 6, Berlin 12489, Germany
E-mail: norbert.koch@physik.hu-berlin.de
Dr. T. Lenz, N. Kotadiya, G. Glasser, Dr. R. Berger,
Prof. P. W. M. Blom, Prof. D. M. de Leeuw
Max Planck Institute for Polymer Research
Ackermannweg 10, Mainz 55128, Germany

Dr. T. Lenz, Prof. P. W. M. Blom
Graduate School Materials Science in Mainz
Staudinger Weg 9, Mainz 55128, Germany
Prof. D. M. de Leeuw
Faculty of Aerospace Engineering
Delft University of Technology
Kluyverweg 1, Delft 2629 HS, The Netherlands

The ORCID identification number(s) for the author(s) of this article can be found under https://doi.org/10.1002/admi.201700324.

1700324 (1 of 8)

ADVANCED
SCIENCE NEWS
www.advancedsciencenews.com

ADVANCED
MATERIALS
INTERFACES
www.advmatinterfaces.de

We start by recalling that Φ of a surface is often defined as the energy needed to bring an electron from the sample to the vacuum level just above the surface.[12–15] In a UPS experiment, the sample is irradiated with an ultraviolet photon beam, and photoelectrons are emitted from the surface due to the photoelectric effect.[16,17] By measuring the kinetic energy (E_{kin}) distribution of the photoelectrons with an energy analyzer, one obtains direct information about the valence electronic structure, mostly from the higher E_{kin} part of the spectrum. The work function is determined by examining the low E_{kin} part of the spectrum, dominated by inelastically scattered electrons. These secondary electrons appear as a high-intensity tail with a sharp cut-off, corresponding to the electrons that have just enough energy to leave the sample.[18] It is this secondary-electron cut-off (SECO) that is used to determine the Φ following the relation $\Phi = h\nu - W$, where W is the width of the UPS spectrum taken from the Fermi level to the SECO and $h\nu$ is the photon energy.[12]

This procedure of measuring Φ is indeed reliable for homogeneous surfaces, such as clean metal surfaces. The different Φ for different crystalline surface orientations can be easily measured.[19,20] For heterogeneous surfaces, which exhibit locally varying Φ, the situation is less clear and not unequivocally understood. For instance, most studies only consider one SECO corresponding to one area-averaged (or macroscopic) work function value.[12,21–26] However, UPS measurements on heterogeneous surfaces often reveal more than one SECO or broad spectral distribution.[9–11] Recently, Sharma et al. studied heterogeneous indium-tin-oxide/Au and nanoroughened, sol–gel-derived, polycrystalline ZnO surfaces by UPS. These measurements revealed that contributions to the SECO are not

proportional to the compound fraction on the surface and that the lower Φ material dominates the SECO shape.[27,28] Clearly, the underlying fundamental mechanisms governing the emergence of multiple cut-offs need to be unraveled. Specifically, we need to understand under which conditions, e.g., for which lateral dimensions and patterns, one or more cut-offs will emerge in a SECO spectrum, and whether Φ values from inhomogeneous surfaces are indeed quantitatively area-averaged.

To tackle these issues, we examined well-defined heterogeneous surfaces with Φ varying periodically by ≈1 eV. These surfaces consist of (i) bilinear arrays of self-assembled monolayers (SAMs) on gold with 4 µm periodicity as schematically shown in **Figure 1**a and (ii) gold–aluminum bilinear arrays with several hundred micrometer periodicity. Microcontact printing[29–31] was used as patterning technique for fabricating the SAM bilinear arrays (Figure S1, Supporting Information). Those were made of 1-hexadecanethiol (CSH) and 1H,1H,2H,2H-perfluorodecanethiol (FSH), which have oppositely oriented dipole moments on gold[32,33] and can therefore be employed to obtain a well-defined Φ modulation when arranged in a bilinear array.

For these model systems, the UPS spectra systematically show two SECOs, which are not just a superposition of the spectra of the two pure single-component surfaces. We explain that this is intrinsically related to the working principle of UPS: in order to contribute to the SECO spectrum, a secondary electron does not only have to escape the sample, but it also has to pass the electrostatic potential landscape between the surface and the analyzer. More specifically, it is found that the electrostatic potential due to the high Φ areas strongly impacts the electrostatic landscape above the low Φ areas. This results in an additional potential barrier above the low work function
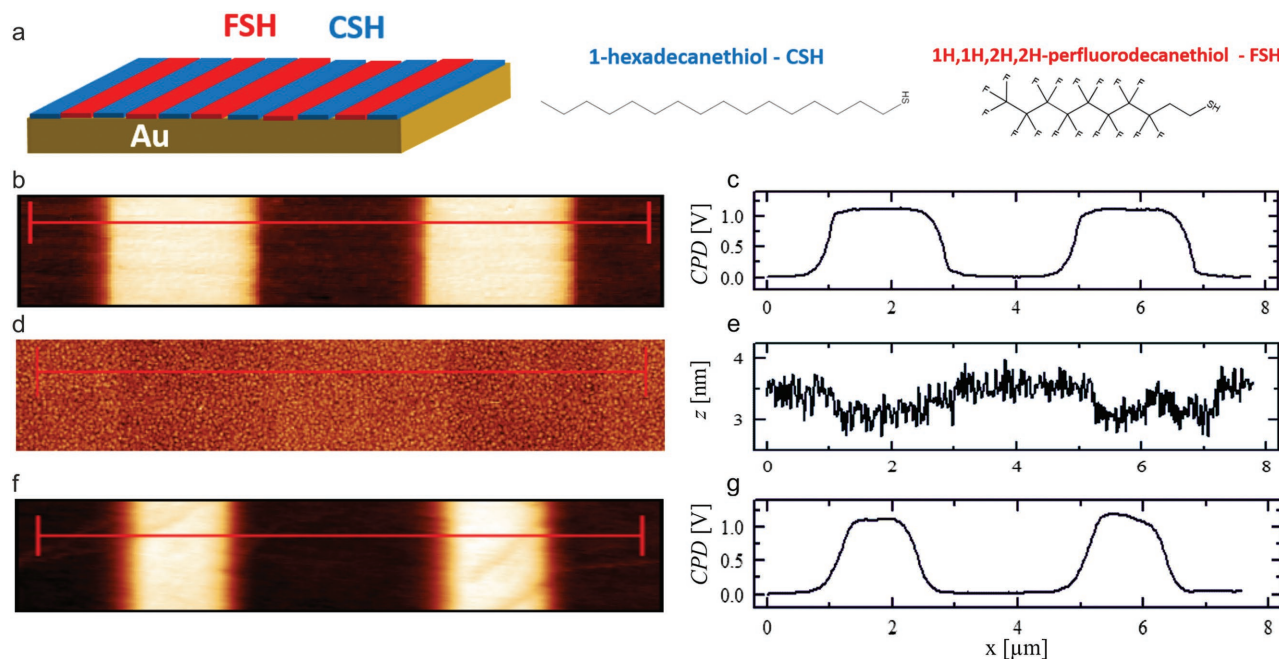

Figure 1. a) Schematic illustration of a bilinear sample structure. Both SAMs are shown on the right. b,c) The KPFM potential map and the corresponding potential line profile for a symmetric sample with 2 µm line width, showing clear separation between the CSH and FSH stripes and a large work function difference of ≈1.1 eV (CPD of CSH was set to 0 for better comparison). d,e) The appropriate height images, indicating a height difference of less than 1 nm between the two SAMs. f,g) The KPFM results for an asymmetric sample are shown, confirming a CSH to FSH ratio of ≈5/3.

areas only and leads to an apparent averaged work function. This is supported by electrostatic modeling and Kelvin probe force microscopy (KPFM), and we provide a comprehensive model that allows predictions on how lateral surface variation and dimensions, as well as the bias applied to the sample, together determine the SECO spectrum, which enables increased confidence in material parameters derived from UPS studies.

2. Results and Discussion

2.1. Experimental Results

An important parameter for microcontact printing is the time of conformal contact between the stamp soaked with thiol and the sample. Symmetric bilinear arrays with a periodicity of 4 µm were fabricated by CSH stamping for 50 s followed by FSH backfilling. Additionally, an asymmetric array with 4 µm periodicity and a CSH/FSH area ratio of ≈5/3 was produced by stamping CSH for 10 min. Figure 1a shows a scheme of the symmetric bilinear array of CSH and FSH SAMs as well as the chemical structures of CSH and FSH. As displayed in Figure 1b–e, frequency modulated (FM) KPFM was used to measure the contact potential difference (CPD) and topographic maps of the 4 µm bilinear arrays. The bright regions of the CPD map correspond to FSH and the dark regions to CSH, respectively. The extracted line profile demonstrates a sharp transition between the two regions and a work function difference of about 1.1 eV. We also note that the corresponding topography images presented in Figure 1d,e show a difference in height between the two SAMs of <1 nm. Therefore, any remaining crosstalk of topography with the CPD signal can be neglected. The measured CPD contrast is in excellent agreement with the work function difference for pristine CSH ($\Phi_{CSH} = 4.4$ eV) and FSH ($\Phi_{FSH} = 5.5$ eV) SAMs on gold as obtained by UPS (see **Figure 2**). The KPFM results for the asymmetric bilinear array are shown in Figure 1f,g. It can be clearly seen that the CSH regions are larger and the FSH regions smaller as compared to the symmetric arrays shown in Figure 1b,c, while the same CPD is maintained.

The SECO spectra of the 4 µm symmetrically and asymmetrically patterned samples are shown in Figure 2a together with the reference SECO spectra of the pristine SAMs in Figure 2b for comparison. The full-range spectrum is shown in the inset, indicating that the SECO features are much sharper than features in the valence band region. For both patterned samples, two SECOs are observed. The intensity of the low E_{kin} SECO located at 4.95 eV for the symmetric arrays and at 4.7 eV for the asymmetric arrays dominates the spectra, as materials with lower work functions have a higher secondary-electron yield.[34–36] This is in good agreement with the relative intensities measured for pristine CSH and FSH samples, shown to scale in Figure 2b for comparison. The high E_{kin} SECO, which appears as an asymmetric shoulder, is located at ≈5.5 and 5.4 eV for the symmetric and asymmetric arrays, respectively. Interestingly, the SECO at higher E_{kin} is at the same energy as that of pure FSH SAMs (see Figure S2 in the Supporting Information for detailed fits). In contrast, the low E_{kin} SECO is
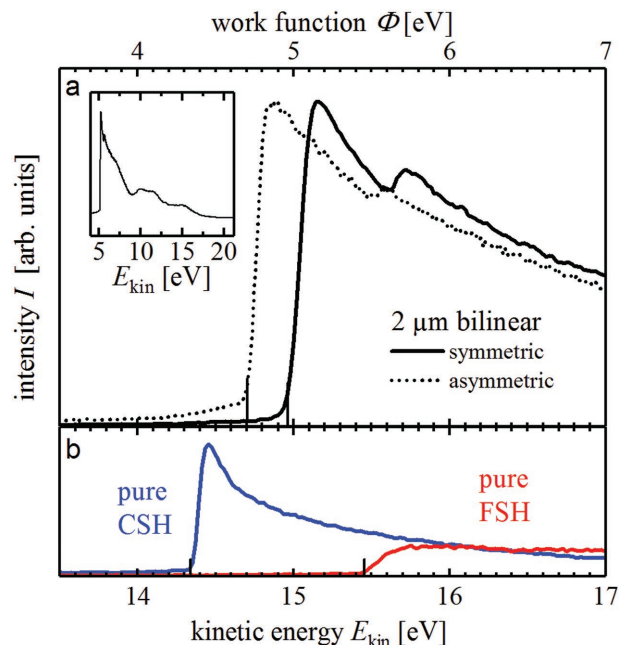

Figure 2. a) SECO spectra of symmetric and asymmetric 2 µm samples. The low kinetic energy cut-off is clearly shifted compared to pure CSH (reference spectra of pristine SAMs shown to scale in b)), whereas the high kinetic energy cut-off is at the same position as the one from the pristine FSH. For the asymmetric sample (larger CSH area), the low kinetic energy cut-off is shifted to lower kinetic energies. For detailed fitting, see Figure S2 in the Supporting Information. The full-range spectrum is shown in the inset in (a). The cut-off features are clearly sharper than the valence band features. A −10 V bias was applied for all measurements.

observed at 0.5 eV (symmetric array) and 0.3 eV (asymmetric array) higher E_{kin} than the SECO of the pure CSH SAMs. Therefore, the observed SECO spectra of the patterned samples are not simply a superposition of the pure reference spectra but consist of (a) a SECO reflecting the pure high Φ material (FSH on Au) and (b) a SECO due to the low Φ material whose energy E_{Lkin} corresponds to an area-averaged sample work function such that $E_{Lkin} = a \cdot \Phi_{CSH} + (1 - a) \cdot \Phi_{FSH}$, where a is the percentage of area covered with CSH.[26] Equivalent results were obtained for samples with a smaller periodicity of 1.2 µm (Figure S3, Supporting Information), supporting the expected length-scale invariance (at least) in the micrometer regime. Further details about length-scale dependence will be provided in the next section. It is important to point out that the SECO spectra do not consist only of a single, averaged SECO as often proposed in literature. The fact that the SECO at high Φ is often missed or disregarded in UPS analysis of heterogeneous surfaces might be due to its low relative intensity,[27] as high Φ materials exhibit notoriously low secondary-electron yields.[37] Moreover, we want to mention that the width of the transition region between CSH- and FSH-covered areas and the corresponding work function change is expected to play a role for the shape and the observation of a second SECO in the spectrum. If the transition region is not sharp, a spatially distributed continuous range of intermediate work functions will lead to a blurred SECO spectrum with no distinct features down to the low Φ cut-off. We suspect this to be the likely reason why in

**ADVANCED
SCIENCE NEWS**
www.advancedsciencenews.com

**ADVANCED
MATERIALS
INTERFACES**
www.advmatinterfaces.de

the SECO spectra of (incrementally deposited) sub-monolayer films, it is common to observe one (low Φ) SECO only.

The energy of the measured two SECOs can be explained by taking into account the potential landscape between the surface and the analyzer as experienced by a secondary electron leaving the sample surface and travelling to the detector. In the present study, this potential landscape is mostly a result of the alternating dipoles of the SAMs on the sample surface. In the next section, we experimentally and theoretically address the potential profile above the surface by means of KPFM and electrostatic calculations in order to determine the potential barrier for the photoelectrons as occurring in an UPS experiment.

2.2. Potential Landscape above the Surface

The UPS SECO provides a measure of the potential barrier experienced by the secondary electrons, but does not provide a detailed picture of the potential landscape. In order to locally determine the electrostatic potential above the sample surface, we performed a series of KPFM measurements with varying tip-sample distances going from 50 to 1200 nm by steps of 50 nm. For the 4 μm symmetric array, the corresponding potential line profiles are displayed as a contour plot in **Figure 3**a, in which the x-axis represents the direction perpendicular to the orientation of the array and the y-axis corresponds to the tip-sample distance. Note that in this graph, the average of each measured potential profile line was set to zero for comparison with electrostatic calculations. At the lateral positions of −4, 0, and 4 μm, the potential is dominated by the CSH SAM stripes positioned below, while at the lateral positions of −2 and 2 μm, the FSH SAM stripes dominate the potential directly above
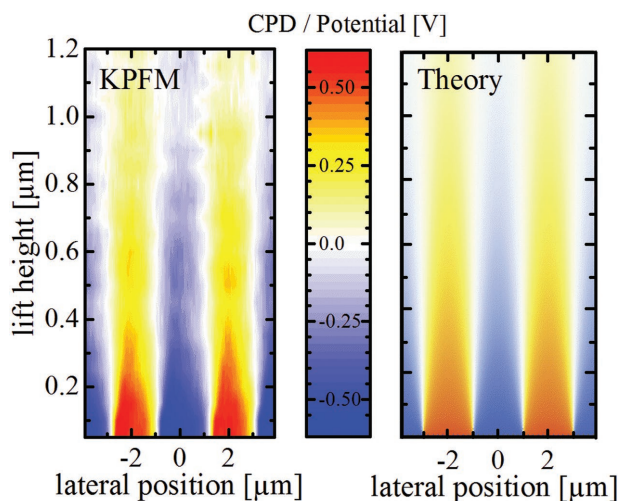

Figure 3. a) Contact potential difference (CPD) between tip and sample obtained from KPFM measurements as a function of position and lift height of the tip. The CSH (blue) and FSH (red) stripes can be clearly differentiated, and the potential converges to an average value for large lift heights. b) The theoretical electrostatic potential above the bilinear array, obtained by solving the Laplace equation, is shown as a function of lateral position and distance from the surface. The dipole difference was set to 1.1 eV for comparison with experiment. The results are in excellent agreement.

the surface. However, with increasing tip-sample distance, the potential approaches an average value above the whole sample surface. This potential mapping can now serve as benchmark for theoretically addressing the electrostatic potential, which is calculated above a periodic arrangement of stripes with different potentials corresponding to CSH and FSH and by solving the Laplace equation (for details, see the Experimental Section and Figure S5, Supporting Information). For comparability, we use a dipole difference of 1.1 eV as obtained from UPS measurements of the reference samples. The calculated potential is presented in Figure 3b and is in excellent agreement with the potential landscape obtained by KPFM. Clearly, this result suggests that the potential far away from the surface converges to an (area) averaged value of the surface potentials above the CSH and FSH stripes.

For the UPS measurements of the symmetric array, this value would correspond to a work function of $\frac{1}{2} \cdot (\Phi_{CSH} + \Phi_{FSH}) = 4.95$ eV, in excellent agreement with the experimental observation (Figure 2a). Theoretically, this means that secondary electrons with energy ranging between 4.4 and 4.95 eV could in principle escape the surface via the CSH-covered regions. However, these secondary electrons will not be able to overcome the increasing barrier above the surface and thus cannot reach the analyzer.

Similarly, in **Figure 4**a, we report the calculated potential (including a −10 V sample bias as usually used in UPS measurements to clear the analyzer work function and a sample/analyzer distance of ≈3.5 cm) above the center of the symmetric CSH and FSH stripes as a function of the distance normal to the sample surface. First, it can be seen that the potential above the FSH stripes decreases continuously away from the surface. This means that the electrons emitted from the FSH stripes have to overcome a potential barrier of 5.5 eV, which is equal to the work function of pristine FSH. In contrast, due to the influence of the potential of the adjacent FSH stripes, the potential above the CSH stripes *increases* away from the surface leading to an additional potential barrier $\Delta\Phi_{CSH}$ of 0.55 eV. Analog calculations for the asymmetric pattern (Figure 4a) show that the potential barrier remains unchanged for the electrons coming from the FSH stripes. For CSH, as a result of spatial averaging, the potential barrier is lowered to ≈4.8 eV (with $\Delta\Phi_{CSH} = 0.4$ eV) as compared to the symmetric structure, in accordance with the UPS measurements (Figure 2a).

In general, this means that the energy of the high work function SECO is independent on the heterogeneity of the surface and is solely determined by the work function of the pristine material, whereas for the low work function areas, electrostatic effects lead to the so-called area-averaging effect.

One interesting question that arises is how this averaging behavior changes with varying feature size. Having demonstrated the good agreement between the electrostatic calculations and the experimental results, one can now investigate theoretically the amplitude of the potential barrier for varying feature sizes and measurement parameters. For work function measurements in UPS, a bias of a few volts is typically applied between the sample and the analyzer, in order to make sure that the secondary electrons can overcome the work function of the analyzer. As shown qualitatively by Helander et al.,[38] this bias results in an electric field that will alter the potential
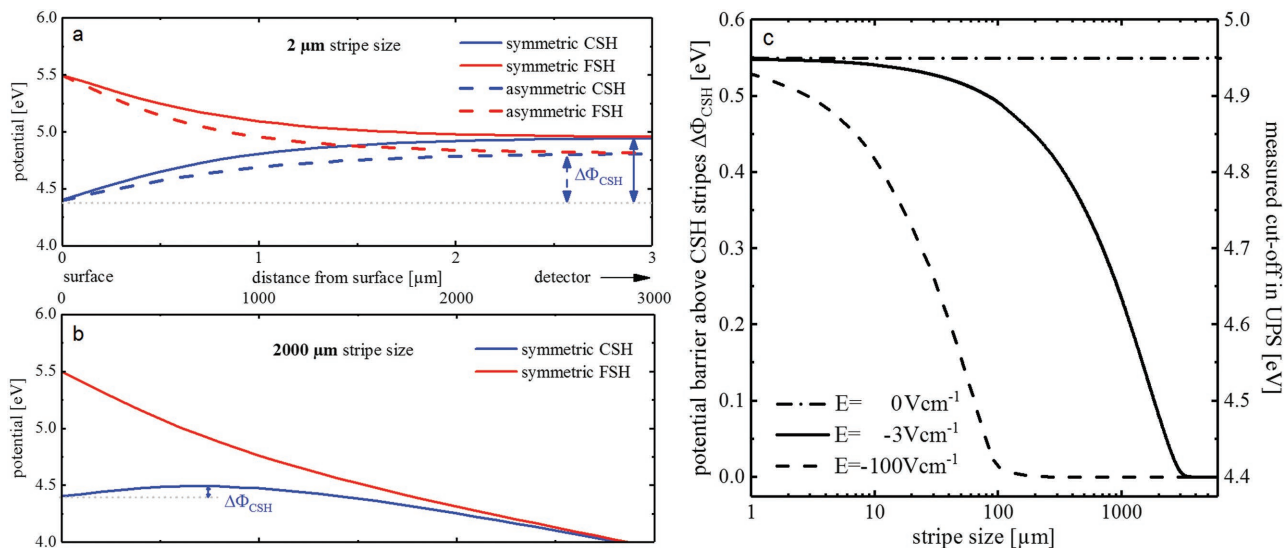
ADVANCED
SCIENCE NEWS
www.advancedsciencenews.com

ADVANCED
MATERIALS
INTERFACES
www.advmatinterfaces.de

Figure 4. a) The calculated potential above the CSH stripes (blue) and the FSH stripes (red) for symmetric (2 μm each, solid lines) and asymmetric (1.5 μm FSH, 2.5 μm CSH, dotted lines) bilinear structures with an applied electric field of −3 V cm^{-1} is shown as a function of distance normal to the surface. Due to the larger CSH area, the potential barrier above the CSH stripes $\Delta\Phi_{CSH}$ is lowered by 150 meV for the asymmetric structure. b) The calculated potential above a symmetric structure with a 2 mm stripe size and the same applied electric field as in (a). The applied electric field lowers $\Delta\Phi_{CSH}$ markedly for this stripe size as compared to (a). c) The potential barrier above the CSH stripes $\Delta\Phi_{CSH}$ as a function of the stripe size is shown for a symmetric bilinear system. The measured work function of the CSH is not changed for stripe sizes larger than 3 mm (for E = −3 V cm^{-1}). For smaller stripe sizes, the measured CSH work function increases due to the influence of the potential landscape, until it converges to an averaged work function for stripe sizes smaller than 10 μm. For higher applied electric fields, the influence of the potential landscape on the measured work function becomes significant only for smaller stripe sizes.

landscape between the sample surface and the analyzer. This additional potential can be easily taken into account in our calculations as a superposition to the potential emerging from the SAM stripes. When including a bias of −10 V and a sample/analyzer distance of 3.5 cm, for the 4 μm patterned samples as in Figure 2a, the resulting potential barrier $\Delta\Phi_{CSH}$ is basically found unchanged as compared to unbiased samples (not shown). In contrast, the bias can play a major role for larger pattern periodicities as exemplarily presented in Figure 4b for a sample with 2 mm stripe size. One can clearly see how the applied electric field impacts the potential and decreases the additional barrier $\Delta\Phi_{CSH}$ (responsible for the apparent averaging effect) above the CSH stripe to only ≈0.1 eV as compared to 0.5 eV for the sample with 2 μm stripe size. This would result in a strong quenching of the averaging effect and a shift of the low kinetic energy SECO to 4.5 eV. In Figure 4c, we present the dependence of the barrier above the CSH stripes as a function of the stripe width (for symmetric samples) when no electric field is involved (zero bias) and for two applied electric fields of −3 and −100 V cm^{-1}. First, without any applied bias, it is found that the potential barrier above the CSH is independent of the stripe width and corresponds to the averaged work function of 4.95 eV (Figure 4c, dash-dotted line). The situation changes noticeably when a sample bias is taken into account, as the potential barrier then varies with stripe width. With an applied field, the curves exhibit three regions as exemplarily discussed for an electric field of −3 V cm^{-1} (Figure 4c, solid line) in the following: (a) for stripe sizes larger than 3 mm, the applied electric field completely compensates the emergence of the potential barrier $\Delta\Phi_{CSH}$ above the CSH stripes, leading to a SECO at 4.4 eV in a UPS spectrum (corresponding to pristine CSH

work function); (b) for decreasing stripe size down to ≈10 μm, the influence of the potential landscape emerging from the striped structure becomes increasingly important, leading to the formation of the potential barrier $\Delta\Phi_{CSH}$, which would shift the low kinetic energy SECO to higher kinetic energies; (c) below 10 μm, the potential barrier $\Delta\Phi_{CSH}$ has reached saturation and the work function as measured in UPS corresponds to the spatially averaged work function amounting to 4.95 eV. For larger electric fields, the influence of the potential landscape on the measured work function in UPS becomes significant for smaller stripe widths, e.g., averaging starts only below 100 μm for an electric field of 100 V cm^{-1} as depicted in Figure 4c (dashed line). These calculations suggest that the measurement parameters, such as applied bias and sample/analyzer distance, should have an effect on the lateral averaging.

To demonstrate the influence of the applied electric field on the measured work function, we fabricated bilinear arrays with either 500–500 μm or 250–200 μm stripe width by evaporating gold on aluminum through shadow masks (due to the lack of stamps with this large size). Such large stripe sizes are indeed needed to clearly observe the influence of the applied bias on the measured SECO (see Figure 4c). The work functions of the pure materials were determined to be Φ_{Au} = 4.50 eV and Φ_{Al} = 3.55 eV after air exposure, in good agreement with the 1 eV work function difference as determined by KPFM on the striped samples (Figure S4, Supporting Information). Selected SECO spectra of the 500–500 μm sample are shown exemplarily for three different biases in **Figure 5**a. It can be seen that, as for the CSH/FSH samples, each spectrum consists of two SECOs at ≈4.5 and ≈3.8 eV due to gold and aluminum, respectively. This first demonstrates, in agreement with the calculations for

**ADVANCED
SCIENCE NEWS**
www.advancedsciencenews.com

**ADVANCED
MATERIALS
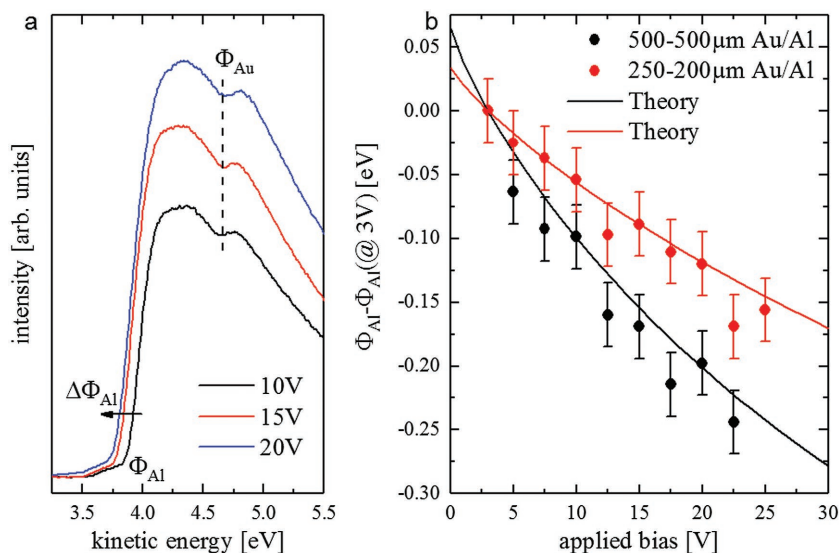INTERFACES**
www.advmatinterfaces.de

Figure 5. a) Secondary-electron cut-off (SECO) of a 500–500 µm Au–Al-striped sample for three different applied biases. The cut-off corresponding to Al shifts to lower kinetic energies with increasing bias, whereas the cut-off corresponding to Au remains constant. b) Work function shift of the Al cut-off (compared to 3 V applied bias) as a function of applied bias for 500–500 µm Au/Al-striped structures (black) and 250–200 µm Au/Al-striped structures (red), both measured (symbols) and calculated (lines).

sample bias of −10 V cm^{-1} as in Figure 4c, that even for such large patterns, an additional potential barrier $\Delta\Phi_{Al}$ (in analogy to $\Delta\Phi_{CSH}$ in Figure 4a,b) still persists but does not result in a fully averaged situation. More precisely, it is found that when increasing the bias, the aluminum-related SECO shifts to lower kinetic energies (after subtraction of the applied bias), while the gold-related SECO remains markedly at constant energy. This shows that the difference in the apparent work function between the two materials is bias-dependent and indicates a reduction of $\Delta\Phi_{Al}$ above the aluminum stripes for increasing external electric field. A summary of the measured aluminum SECO shifts (due to changes in $\Delta\Phi_{Al}$) as a function of applied bias is shown in Figure 5b for both stripe widths. As further displayed in this figure, the change of the potential barrier as calculated from Equation (5) is in excellent agreement with the experimental results. This clearly demonstrates the influence of the applied bias on the SECO measurements by UPS on heterogeneous surfaces.

3. Conclusion

We fabricated model work function-patterned surfaces with lateral periodicity ranging from 4 µm to 1 mm and ≈1.1 eV Φ difference. These heterogeneous Φ surfaces were characterized by UPS and KPFM experiments. In contrast to the common assumption that heterogeneous surfaces should show only one area-averaged SECO in UPS, two SECOs appear. We explain this phenomenon and find that the high E_{kin} SECO provides an accurate measure of the high Φ material. In contrast, the low E_{kin} SECO is not representative of the low Φ material, but exhibits a value that depends on the low/high Φ materials area ratio. The twofold SECO energies are explained by the

electrostatic potential distribution above the surface. Notably important is the influence of the high Φ areas, which gives rise to an additional potential barrier $\Delta\Phi$ above the low Φ areas that have to be overcome by the secondary electrons and lead to a shift of the SECO to higher kinetic energies. This potential above the surface was investigated experimentally with KPFM by performing potential line scans for varying tip-sample distance. Theoretical modeling of this potential shows very good agreement with the experimentally determined one. In addition, using samples with periodicities of a few hundred micrometer, it is experimentally and theoretically demonstrated that increasing the sample bias decreases the averaging effect by lowering the additional energy barrier $\Delta\Phi$. This also demonstrates the generality of our results. These findings have major implications for the reliable interpretation of work function measurements with UPS, particularly for multicomponent inhomogeneous surfaces and micro- to nanostructures. First, Φ measurements are an important part of determining the origin of electrostatic potential changes across an interface formed by electronic materials, and therefore understanding Φ variation as surface composition-dependent parameter is crucial. Second, reliable Φ values are essential to derive meaningful ionization energy and electron affinity values of materials, which directly impact the quality of material selection during the design of electronic and optoelectronic devices.

4. Experimental Section

Materials: Sylgard 184 silicone elastomer together with the curing agent for standard polydimethylsiloxane (PDMS) stamps were purchased from Dow Corning (USA). For the preparation of composite or so-called h-PDMS ("hard" PDMS)[39] stamps, following chemicals were purchased from abcr (Germany): vinylmethylsiloxane-dimethylsiloxane trimethylsiloxy terminated copolymer, viscosity 800–1200 cSt, 7–8 mol% vinylmethylsiloxane (CAS: 67762-94-1); platinum–divinyltetramethyldisiloxane complex in xylene (2.1–2.4% Pt, CAS: 68478-92-2); 1,3,5,7-tetravinyl-1,3,5,7-tetramethylcyclotetrasiloxane (CAS: 2554-06-5); (25–35% methylhydro-siloxane)–dimethylsiloxane copolymer, viscosity 25–35 cSt (CAS: 68037-59-2).

CSH and FSH were purchased from Sigma Aldrich. Ethanol, toluene, and 2-propanol were analytical grade purchased from VWR chemicals. Thiol solutions with desired concentrations were prepared using ethanol as a solvent.

Substrate Preparation: Silicon wafers with thermally grown oxide were cut into of 3 × 3 cm^2 pieces and served as substrates. The substrates were cleaned in ultrasonic bath for 5 min in both acetone and isopropanol. Subsequently, they were dried and transferred to the evaporation chamber. After deposition of 2 nm of Cr as adhesion layer (rate of ≈0.2 Ås^{-1}), 100 nm of Au were evaporated at the rate of ≈5 Ås^{-1} in a dynamic vacuum of 2×10^{-7} mbar. The substrates were then used for microcontact printing without any further surface treatment.

Bulk SAM Preparation: Bulk grown SAMs serve as reference for microcontact printing. They were prepared by immersing substrates in either CSH solution (0.1×10^{-3} M) or FSH solution (10×10^{-3} M). The

**ADVANCED
SCIENCE NEWS**

www.advancedsciencenews.com

**ADVANCED
MATERIALS
INTERFACES**

www.advmatinterfaces.de

same concentrations were chosen as used for microcontact printing. After 24 h, the substrates were taken out of the solution and rinsed with ethanol, toluene, and 2-propanol, and blown dry using nitrogen. It was noted that the immersion time is not critical. A high-quality SAM could already be achieved after 1 h. All the preparations were performed in ambient.

Microcontact Printing of CSH-FSH SAMs Bilinear Arrays: In order to prepare bilinear arrays of CSH and FSH SAMs, a h-PDMS stamp was immersed in CSH solution (0.1×10^{-3} M). After 1 h, the stamp was blown dry and then brought in conformal contact with the substrate. Gentle pressure was manually applied. In the contact regions, CSH molecules diffused from the h-PDMS stamp to the substrate and self-assembled on the Au. After ≈50 s, the h-PDMS stamp was manually detached, before the substrate was rinsed with ethanol, toluene, and 2-propanol to remove any loosely attached molecules.[40] In the second step, the patterned substrate was immersed in FSH solution (10×10^{-3} M) to backfill the remaining uncovered Au surface.[41] After 1 h, the substrate was rinsed again with ethanol, toluene, and 2-propanol and blown dry.

Aluminum–Gold Bilinear Arrays: Al–Au-striped samples were fabricated by first depositing an aluminum film from a metal boat on a glass substrate. A 10 nm gold film was then evaporated on the Al sample through a shadow mask. The pressure during evaporation of both materials was in the 10^{-6} mbar range. The samples were exposed to air before being measured by UPS and KPFM.

KPFM: KPFM on bilinear arrays was performed using a Bruker Dimension Icon Scan. The instrument was operated in PeakForce KPFM mode. This mode performed measurements using FM and lift mode. All the measurements were performed using SCM-PIT probes, which had a steep tip with platinum–iridium coating. The tip diameter is 20 nm and the cantilever spring constant is 2.8 Nm^{-1}. The sample was grounded by electrically connecting the Au electrode to the chuck using copper tape. The standard lift scan height for all samples was 60 nm.

UPS: All UPS measurement were conducted at the Humboldt Universität zu Berlin, using a multitechnique UHV apparatus consisting of an interconnected sample preparation and analysis chamber (base pressures of 1×10^{-9} mbar and 1×10^{-10} mbar). For excitation, the He I radiation of a helium gas discharge lamp (21.21 eV) was used and the photoelectrons were detected using a Phoibos 100 hemispherical energy analyzer. The resolution of the analyzer was determined by measuring the Fermi-edge of a clean gold crystal and was about 0.2 eV for the setting used in this study. The SECOs were measured with an applied bias of −10 V to clear the analyzer work function and a sample/analyzer distance of ≈3.5 cm. The sample was perpendicular to the analyzer during the measurements, which is crucial according to Helander et al [38]. The finite acceptance angle of the analyzer (<15°) does not influence the obtained results.

The different work functions of the samples were determined by fitting the SECOs according to

$$I_{SECO}(E) \sim H(E - E_0) \times G(E) e^{-aE} \tag{1}$$

where $H(E - E_0) \times G(E)$ was the convolution of a Heaviside step function with a Gaussian function, which accounted for the steep rise in intensity for kinetic energies higher than the work function, and e^{-aE} accounted for the background. A similar expression was suggested by Ogawa et al.[42] and had proven to work well for determining the work function from SECO spectra. For more complex systems, like the ones investigated in this study, the background is more complicated. However, this formula could still be used to determine the different work functions with a reasonable precision (≈50 meV). The work function was determined from the intersection of a linear extrapolation of the steep edge with the background as typically done in photoelectron spectroscopy.

Electrostatic Modeling: The theoretical electrostatic potential $\varphi(x,z)$ of a bilinear array with periodicity L, an area ratio between the different potentials η, and a negative applied bias ΔV between the sample and the analyzer (see Figure S5 in the Supporting Information for illustration) was derived by solving the Laplace equation

$$\Delta\varphi(x,z) = 0 \tag{2}$$

with the Dirichlet boundary conditions

$$\varphi(x,0) = \Delta\Phi\, pulse(L,\eta) \tag{3}$$

$$\varphi(x,d) = \Delta V \tag{4}$$

where $\Delta\Phi$ was the WF difference between the two SAMs (1.1 eV, taken from UPS reference measurements), $pulse(L,\eta)$ was a pulse function with the periodicity L and a potential area ratio η, and ΔV was the applied voltage between the sample and the analyzer at distance d. The solution of Equations (2)–(4) was derived by using the method of *separation of variables* as described in detail for example by Olver.[43] For the Laplace equation in Cartesian coordinates, this yielded the general solution

$$\varphi(x,z) = \sum_{n=1}^{\infty} b_n \frac{\sinh\left(\dfrac{2n\pi(d-z)}{L}\right)}{\sinh\left(\dfrac{2n\pi d}{L}\right)} \tag{5}$$

where the coefficients b_n were given by the Fourier series of the boundary condition (3). For a pulse function, this is given by

$$b_n = \Delta\Phi \cdot \eta + \sum_{n=1}^{\infty} \frac{2\Delta\Phi}{n\pi} \sin(n\pi\eta) \cdot \cos\left(\frac{2\pi n x}{L}\right) \tag{6}$$

Combining Equations (5) and (6) and a linear potential $\frac{\Delta V}{d} z$ resulting from the applied bias between sample and analyzer, a final result shown below was obtained for the potential above a periodic work function pattern

$$\varphi(x,z) = \frac{\Delta V}{d} z + \Delta\Phi \cdot \eta$$
$$+ \sum_{n=1}^{\infty} \frac{2\Delta\Phi}{n\pi} \sin(n\pi\eta) \cdot \cos\left(\frac{2\pi n x}{L}\right) \cdot \frac{\sinh\left(\dfrac{2n\pi(d-z)}{L}\right)}{\sinh\left(\dfrac{2n\pi d}{L}\right)} \tag{7}$$

For calculations shown in this work, $n = 100$ was used, which was found to yield converged solutions.

Supporting Information

Supporting Information is available from the Wiley Online Library or from the author.

Conflict of Interest

The authors declare no conflict of interest.

[1] H. Alves, A. S. Molinari, H. Xie, A. F. Morpurgo, *Nat. Mater.* **2008**, *7*, 574.

[2] L. Huder, C. Rinfray, D. Rouchon, A. Benayad, M. Baraket, G. Izzet, F. Lipp-Bregolin, G. Lapertot, L. Dubois, A. Proust, L. Jansen, F. Duclairoir, *Langmuir* **2016**, *32*, 4774.

[3] W. Chen, D. C. Qi, Y. Huang, H. Huang, Y. Z. Wang, S. Chen, X. Y. Gao, A. T. S. Wee, *J. Phys. Chem. C* **2009**, *113*, 12832.

[4] M. T. Greiner, M. G. Helander, W.-M. Tang, Z.-B. Wang, J. Qiu, Z.-H. Lu, *Nat. Mater.* **2012**, *11*, 76.

[5] P. C. Rusu, G. Giovannetti, C. Weijtens, R. Coehoorn, G. Brocks, *Phys. Rev. B* **2010**, *81*, 125403.

[6] M. Zhang, I. Irfan, H. Ding, C. W. Tang, Y. Gao, *Org. Electron.* **2011**, *12*, 1588.

[7] T. Nishi, K. Kanai, Y. Ouchi, M. R. Willis, K. Seki, *Chem. Phys.* **2006**, *325*, 121.

[8] J. Q. Zhong, H. Y. Mao, R. Wang, D. C. Qi, L. Cao, Y. Z. Wang, W. Chen, *J. Phys. Chem. C* **2011**, *115*, 23922.

[9] L. Aversa, R. Verucchi, R. Tatti, F. V. D. Girolamo, M. Barra, F. Ciccullo, A. Cassinese, S. Iannotta, *Appl. Phys. Lett.* **2012**, *101*, 233504.

[10] A. Tada, Y. Geng, Q. Wei, K. Hashimoto, K. Tajima, *Nat. Mater.* **2011**, *10*, 450.

[11] T. Wang, T. R. Kafle, B. Kattel, Q. Liu, J. Wu, W.-L. Chan, *Sci. Rep.* **2016**, *6*, 28895.

[12] D. Cahen, A. Kahn, *Adv. Mater.* **2003**, *15*, 271.

[13] A. Kahn, *Mater. Horiz.* **2016**, *3*, 7.

[14] R. Smoluchowski, *Phys. Rev.* **1941**, *60*, 661.

[15] E. Wigner, J. Bardeen, *Phys. Rev.* **1935**, *48*, 84.

[16] C. Nordling, E. Sokolowski, K. Siegbahn, *Phys. Rev.* **1957**, *105*, 1676.

[17] D. W. Turner, M. I. A. Jobory, *J. Chem. Phys.* **1962**, *37*, 3007.

[18] M. Yoshitake, W. Song, *J. Surf. Anal.* **2006**, *13*, 185.

[19] A. Goldmann, V. Dose, G. Borstel, *Phys. Rev. B* **1985**, *32*, 1971.

[20] G. V. Hansson, S. A. Flodström, *Phys. Rev. B* **1978**, *18*, 1572.

[21] J. B. Hudson, *Surface Science: An Introduction*, John Wiley & Sons, Chichester, UK **1998**.

[22] S. Hüfner, *Photoelectron Spectroscopy: Principles and Applications*, Springer, Berlin Heidelberg, Germany **2003**.

[23] H. Ishii, K. Sugiyama, E. Ito, K. Seki, *Adv. Mater.* **1999**, *11*, 605.

[24] K. Oura, V. G. Lifshits, A. A. Saranin, A. V. Zotov, M. Katayama, *Surface Science: An Introduction*, Springer, Berlin Heidelberg, Germany **2003**.

[25] M. Prutton, in *Electronic Properties of Surfaces* (Ed: W. J. E. Mitchell), Adam Hilger Ltd., Bristol, UK **1984**.

[26] D. P. Woodruff, T. A. Delchar, in *Modern Techniques of Surface Science* (Ed: A. E. Davis), Cambridge University Press, Cambridge **1994**.

[27] A. Sharma, R. Berger, D. A. Lewis, G. G. Andersson, *Appl. Surf. Sci.* **2015**, *327*, 22.

[28] A. Sharma, M. Untch, J. S. Quinton, R. Berger, G. Andersson, D. A. Lewis, *Appl. Surf. Sci.* **2016**, *363*, 516.

[29] A. Kumar, H. A. Biebuyck, G. M. Whitesides, *Langmuir* **1994**, *10*, 1498.

[30] A. Perl, D. Reinhoudt, J. Huskens, *Adv. Mater.* **2009**, *21*, 2257.

[31] D. Qin, Y. Xia, G. M. Whitesides, *Nat. Protoc.* **2010**, *5*, 491.

[32] D. M. Alloway, M. Hofmann, D. L. Smith, N. E. Gruhn, A. L. Graham, R. C. Jr., V. H. Wysocki, T. R. Lee, P. A. Lee, N. R. Armstrong, *J. Phys. Chem. B* **2003**, *107*, 11690.

[33] B. de Boer, A. Hadipour, M. M. Mandoc, T. van Woudenbergh, P. W. M. Blom, *Adv. Mater.* **2005**, *17*, 621.

[34] G. F. Dionne, *J. Appl. Phycol.* **1975**, *46*, 3347.

[35] X. Li, Z. Zhang, V. E. Henrich, *J. Electron Spectrosc. Relat. Phenom.* **1993**, *63*, 253.

[36] J. J. Scholtz, D. Dijkkamp, R. W. A. Schmitz, *Philips J. Res.* **1996**, *50*, 375.

[37] A. Shih, J. Yater, C. Hor, R. Abrams, *Appl. Surf. Sci.* **1997**, *111*, 251.

[38] M. G. Helander, M. T. Greiner, Z. B. Wang, Z. H. Lu, *Appl. Surf. Sci.* **2010**, *256*, 2602.

[39] T. W. Odom, J. C. Love, D. B. Wolfe, K. E. Paul, G. M. Whitesides, *Langmuir* **2002**, *18*, 5314.

[40] T. Lenz, T. Schmaltz, M. Novak, M. Halik, *Langmuir* **2012**, *28*, 13900.

[41] R. K. Smith, P. A. Lewis, P. S. Weiss, *Prog. Surf. Sci.* **2004**, *75*, 1.

[42] S. Ogawa, Y. Takakuwa, *Surf. Sci.* **2007**, *601*, 3838.

[43] P. Olver, *Introduction to Partial Differential Equations*, Springer International Publishing, Switzerland **2014**.